PHYSICAL REVIEW A VOLUME 49, NUMBER 6 JUNE 1994

Electron emission and image-charge acceleration for the impact of very highly charged ions on clean gold

H. Kurz, F. Aumayr,* and HP. Winter
Institut für Allgemeine Physik, Technische Universität Wien, 1040 Wien, Austria

D. Schneider, M. A. Briere, and J. W. McDonald
Lawrence Livermore National Laboratory, Livermore, California 94551

(Received 23 December 1993)

We present total yields for emission of slow ($E_e \leq 50$ eV) electrons due to the impact of slow ($v_p \leq 5\times10^5$ m/s) highly charged ions [Ar^{q+} ($q \leq 18$), Xe^{q+} ($q \leq 51$), and Th^{q+} ($q \leq 80$)] on clean polycrystalline gold. The highly charged ions were produced in the Lawrence Livermore National Laboratory electron-beam ion trap; electron yields have been derived from the respective measured electron emission statistics. The experimental data support a currently accepted scenario for multicharged ion-induced electron emission, which is largely based on a classical over-barrier model. In particular, we are able to distinguish different processes contributing to the total above-surface electron emission. In addition, an ultimate low-impact-energy limit due to projectile self-acceleration toward the metal surface, as a result of the projectile image charge, has been demonstrated and evaluated.

PACS number(s): 79.20.Nc, 31.50.+w, 79.90.+b

I. INTRODUCTION

In the present work, we will deal with total yields for emission of slow ($E_e \leq 50$ eV) electrons due to the impact of slow ($v_p \leq 5\times10^5$ m/s) highly charged ions Z^{q+} on a clean gold surface. By the term "highly charged" we like to characterize multicharged ions (MCI's) which for their production require a total ionization energy considerably higher than the kinetic energy with which they bombard the target surface.

The impact of MCI's on a solid surface can initiate, among other processes, ejection of electrons due to both potential emission (PE) and kinetic emission (KE) [1]. These two principally different processes are of considerable practical relevance for, e.g., plasma-wall interaction in gas discharges, thermonuclear fusion experiments, ion-beam-activated material modification and surface analytics by means of ion-beam scattering.

Since the related PE yields generally increase with the potential energy $W_{q,\mathrm{pot}}$ carried by a MCI Z^{q+}, and since for $v_p < 1$ a.u. (25 keV/amu) the KE yields generally decrease with decreasing v_p, PE will be the predominant electron emission process at sufficiently low v_p and/or high $W_{q,\mathrm{pot}}$ [1]. Studies of PE due to the impact of MCI's on clean metal surfaces have been pioneered by Hagstrum ($q \leq 5$; [2–4]) and by Arifov *et al.* ($q \leq 8$; [5]), who investigated both the related total electron yields and the energy distributions of ejected electrons. Later on, similar work has been performed with higher charged ions as, e.g., Ar^{q+} ions up to $q=12$ [6–11]. There, it was shown that for Ar ions in charge states $q>8$ the resulting total electron yields did not further linearly increase according to the MCI total recombination energy, as had to be expected from the behavior for lower ion charge states [2–5], the reason for this deviation being the following. During the MCI's approach toward the surface, its neutralization primarily takes place by resonant electron transitions from the target valence band into highly excited Rydberg states on the projectile. If an ion initially carries one or several vacancies in its inner shells, they will survive until close contact with the target surface or even into the target bulk. There, they can recombine under emission of fast Auger electrons, as demonstrated from the related above- and below-surface Auger electron spectra [12–20], and/or by emission of soft x rays [21–26]. Sometimes inner-shell vacancies in primary MCI's can even survive the projectile scattering [27] or become transferred into sputtered, secondary ions from the target [28]. Increasingly detailed reviews of this now rapidly emerging field have been given by a number of authors [1,29–33].

The classical over-the-barrier (COB) model for ion-surface interaction developed by Burgdörfer *et al.* [34–36] provides a simple description of electron capture, partial deexcitation of the transiently formed hollow atoms, and the various electron-emitting processes occurring until surface impact. For ions in medium charge states ($q \leq 16$), calculations based on the COB model showed good agreement with both measured total electron yields [37] and emission statistics (ES) probability distributions [38]. According to the COB model—while the projectile is sufficiently far from the surface—the electrons experience a potential barrier between the surface and the projectile, which is formed by the projectile's (screened) Coulomb potential, the projectile's image po-

---

*Corresponding author.
Electronic address: aumayr@eapv38.tuwien.ac.at
FAX: (+43-1)564203.

tential, and the image potential of the electron itself. As the projectile ion approaches the surface, the barrier height will decrease and drop below the Fermi level at a critical distance,

$$R_c(q)=\frac{1}{2W_\phi}\sqrt{8q+2}\approx\frac{\sqrt{2q}}{W_\phi} \qquad (1)$$

(W_ϕ is the work function of the target and atomic units are used unless otherwise stated). Consequently, at and beyond $R_c(q)$ electrons from the conduction band can be captured resonantly into highly excited states of the projectile. This resonant neutralization (RN) together with its inverse process [resonant ionization (RI), i.e., resonant transition of an electron from the projectile into an empty state above the Fermi level in the conduction band of the target] proceed whenever the condition $R<R_c$ is satisfied for the successively decreasing projectile charge q. At the same time, electrons bound on the projectile become subject to Auger-type processes, which may excite them above the vacuum level in order to contribute to electron emission ["autoionization," (AI)], or they can be transferred into empty states above the Fermi level in the conduction band ["Auger loss to conduction band," AL]. The screening of the charge of the ion core by electrons already occupying lower levels as a result of preceding RN-AI processes and interaction with the image charge of the ion core will shift the projectile energy levels upwards and may also promote electrons bound in such states above the vacuum level, such that they will contribute to the electron emission. Finally, electrons still bound in highly excited projectile levels with Rydberg radii exceeding the screening length in the metal will be "peeled off" as soon as the projectile reaches the surface. This process and the subsequent reneutralization of the ion into lower excited states result in the formation of a modified hollow atom inside or just at the metal surface. The relaxation of this hollow atom produces fast subsurface Auger electrons [12–20], which also can cause emission of slow secondary electrons, with the latter contributing to the measured slow electron yields. Alternatively, relaxation of the hollow atom inside the solid can also take place via radiative transitions (emission of soft x rays [21–26]).

II. EXPERIMENTAL SETUP AND DATA EVALUATION

In this paper we will regard emission of slow (typically $E_e \leq 50$ eV) electrons due to the impact of slow, highly charged ions on clean gold. Measurements of the slow electron emission statistics, from which related total electron emission yields presented in this work have been obtained, were performed with an experimental method developed by us over the past few years [39–41]. Beams of ions Z^{q+} with kinetic energies of several q keV are directed via a four-element cylindrical electrostatical lens, which accelerates or decelerates the ions by a variable potential of up to ±3 kV toward an atomically clean polycrystalline gold target under perpendicular incidence. Electrons emitted from the target surface are deflected and turned around by 96% transparent conical electrode, and by means of another three-element lens they are extracted from the target region and accelerated and focused onto a surface-barrier detector where they arrive with a kinetic energy of about 25 keV [40]. The resulting pulses are amplified and shaped and the pulse-height spectra are recorded by a multichannel analyzer.

The target surface was regularly sputter cleaned with 2-keV Ar^+ ions, in order to prepare and maintain an atomically clean surface. A turbomolecular pump and a Ti-sublimation pump with a liquid nitrogen-cooled baffle kept the background pressure in the detector region below 3×10^{-8} Pa during all measurements. The detector assembly and the usually applied evaluation procedure have been described in more detail elsewhere [37,39,41,42].

The highly charged ions applied in this work were produced with the electron-beam ion trap (EBIT) at Lawrence Livermore National Laboratory [43–45]. In this MCI source, an electron beam (3 keV $\leq E_{\mathrm{kin}} \leq 20$ keV, $I_{\mathrm{el}} \leq 240$ mA, $d\approx70$ μm) is compressed by an axial magnetic field ($B\leq3$ T) within a super-conducting solenoid and three cylindrical drift tubes, where it ionizes the present atoms or molecules. The resulting ions are trapped in radial direction by the space charge of the electron beam and in axial direction by suitable electric potentials applied to the drift tubes. Electron-impact ionization increases the ion charge states step by step during a preselectable time, leading to a corresponding equilibrium charge state distribution. If then the axial potential barrier which confines the ions to the center drift tube is lowered, the ions can be extracted from the trap. For most of the measurements presented here, the ion extraction potential was 3 kV; for heavier ions we also used up to 7 kV.

After passing an Einzel lens, an electrostatical bender, a second Einzel lens, and a set of collimating slits, the ions were analyzed according to q/m by a 90° bending magnet, and then collimated again by a set of two four-jaw slits (2×2 mm^2, ≈2 m apart) before entering the deceleration-target-detector assembly described above.

The space charge of the electron beam in the ion trap lowers the effective extraction potential experienced by the ions by an amount of approximately 60–80 V, depending on the extracted ion species and the different operating parameters of the EBIT. Consequently, the actual kinetic energy of the ions had to be determined for each projectile and each set of ion source parameters by measuring the ion count rate at the target as a function of the decelerating potential applied to the target and the surrounding electrodes (as an example, see data for Th^{71+} sketched by full symbols in Fig. 1). Numerical differentiation of the resulting smoothed curve yielded the related ion-beam energy profile (solid line in Fig. 1). By means of tight collimation of the ion beam and exact alignment of the deceleration lens assembly, and also making use of ray tracing calculations, we could assure that steering and/or defocusing effects of the deceleration lenses had no influence on the observed energy spread of the ion beam.

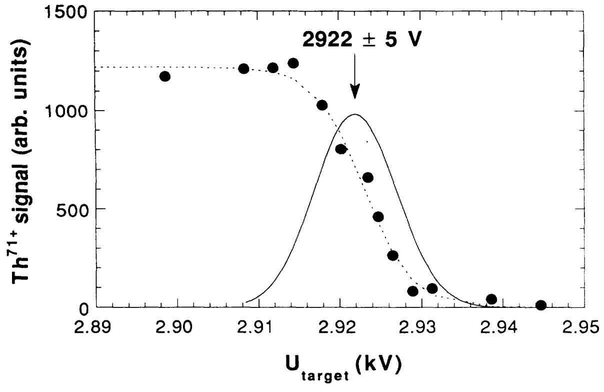

FIG. 1. Determination of kinetic energy of slow ions extracted from EBIT. The count rate at the ES detector has been plotted vs deceleration voltage (i.e., potential of the target and the last element of the cylinder lens) for impact of Th^{71+} on Au (full symbols). The solid line shows the energy profile of a beam of Th^{71+} ions, as obtained by differentiating the above described smoothed data. The difference of ≈ 78 V between the ion source potential of 3 kV and the centroid of the ion-beam energy profile is ascribed to the space charge of the ionizing electron beam in EBIT. Variation of the current, energy, and focusing of these electrons has a strong influence on both the mean energy and the energy spread of the ion beam.

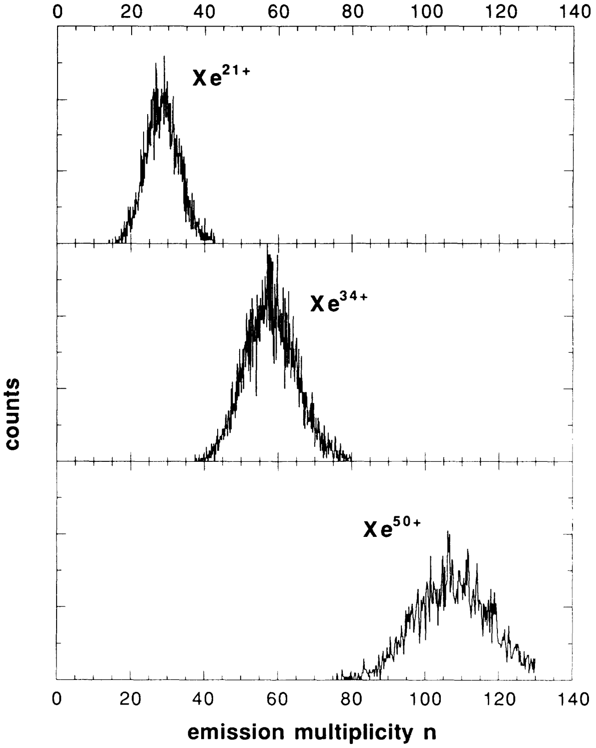

FIG. 2. Typical pulse-height spectra measured with the electron detector for impact of highly charged Xe ions on a polycrystalline gold target at a projectile velocity $v_p \approx 5\times10^5$ m/s. The unit on the horizontal axis is the electron-emission multiplicity, i.e., the number of electrons emitted due to one impinging projectile.

Figure 2 shows some examples for pulse-height spectra from different highly charged Xe^{q+} ions impinging on clean Au. For electrons yields $\gamma \geq 20$, inelastic backscattering of electrons from the detector surface dominates these spectra and smears out the structure of equidistant peaks at multiples of 25 keV. The determination of the emission statistics (ES—i.e., the distribution of emission probabilities W_n for a given number of n electrons—by fitting a linear combination of peak shapes accounting for electron backscattering [39,41] to these spectra became both time consuming and numerically unstable, so that a more suitable evaluation method had to be developed.

Similar measurements with projectiles in lower charge states [38,46] have shown that the probability distributions for slow MCI-induced electron emission are smooth and very close in shape to Gaussians, and so are the related pulse-height spectra. With $\gamma_{\rm ES}$ being the total electron yield (i.e., the average number of electrons emitted by one projectile particle), p_r the probability that an electron is backscattered from the active surface of the solid-state detector, and k_r the fraction of the original energy carried away by this backscattered electron, the mean value α of the pulse-height spectrum should result from the sum of $(1-p_r)1\gamma_{\rm ES}$, viz., the contribution of electrons depositing their full kinetic energy, and $p_r(1-k_r)\gamma_{\rm ES}$, viz., the contribution of backscattered electrons that deposit only a fraction $(1-k_r)$ of their kinetic energy in the active layer of the solid-state detector,

$$\alpha=\{1-p_r+(1-k_r)p_r\}\gamma_{\rm ES}=(1-k_rp_r)\gamma_{\rm ES}\ . \qquad (2)$$

To test Eq. (2), we simulated pulse-height spectra as linear combinations of known peak shapes [39] by assuming Gaussian probability distributions with mean values $\gamma_{\rm ES}$ and different standard deviations, and choosing different values for p_r, k_r, determined mean values α, and standard deviations of Gaussians fitted to these spectra. We found that Eq. (2) holds very well for a wide range of yields $\gamma_{\rm ES}$ $(20\leq\gamma_{\rm ES}\leq360)$, essentially independent of the widths of the Gaussian distributions used to simulate the spectra. The same proportionality [Eq. (2)] was also found for the standard deviations of the probability distributions and the simulated spectra. To finally evaluate the measured spectra, the values $p_r=0.155$ and $k_r=0.6$ (determined experimentally as well as by ray tracing calculations [39,47]) have been adopted. The uncertainty for the total slow electron yields determined in the way just described has been estimated to be about ±4% (cf. also [37]).

A highly charged ion is accelerated toward a conducting surface by its image charge and thus gains a considerable amount of kinetic energy (in the order of $\Delta E_{q,\rm im}\approx q^{3/2}$ eV [34], cf. also Sec. III E below). Therefore, throughout this paper the term "nominal" projectile velocity refers to the velocity of the ions as calculated from the difference between the potential of the ion source and the target, i.e., the chosen projectile velocity before the image charge has further accelerated the projectile ion.

III. EXPERIMENTAL RESULTS AND DISCUSSION

Evaluation of the above described pulse-height spectra delivered the total electron yields and widths of the ES for impact of various highly charged projectile species (Ar^{q+}, $15 \le q \le 18$, Xe^{q+}, $17 \le q \le 51$, and Th^{q+}, $51 \le q \le 80$) under normal incidence on clean polycrystalline gold. The nominal velocity of these ions has been varied from a few 10^4 m/s up to 5×10^5 m/s, corresponding to kinetic energies from less than 1 eV/amu up to 1.3 keV/amu. A first, limited account of these measurements has been published in Ref. [48].

A. Total electron yields vs projectile charge state

In Fig. 3, total electron yields for two different projectile impact velocities ($v_p \approx 5\times10^4$ m/s and 5×10^5 m/s, respectively) have been plotted vs projectile charge state q. The shown electron yields γ rise almost linearly with increasing q, and up to the highest charge states no saturation of the yields could be observed. As a general trend, for any given ion species at $v_p \approx 5\times10^4$ m/s, about 35% more electrons are emitted than at $v_p \approx 5\times10^5$ m/s. Evidently, even for Th^{80+} the metal surface can deliver rapidly enough up to 340 electrons ($\gamma \approx 260$ electrons are emitted and another 80 electrons are required to neutralize the projectile) within the short time between the ion passing the distance R_c and its complete deexcitation inside the solid. Considering the finite widths of the ES probability distributions, the maximum number of electrons emitted can still be considerably higher. The most extreme example encountered in this work is given for slow Th^{79+} projectiles ($v_p \le 2\times10^4$ m/s), which show a total yield (mean value of ES) of $\gamma \approx 280$ with an ES standard deviation $\sigma \approx 20$, so that about 15% of the projectiles give rise to emission of 300 or more electrons and in total ≥ 380 electrons are extracted from the surface.

We can show that the electronic level structure of the projectile also plays an important role in the electron emission processes. One indication for this is the discontinuity between the yields for different ion species with equal charge (cf. Fig. 3, Ar and Xe at $q = 17$, Xe and Th at $q = 51$). A reason for this discontinuity is the higher potential carried by lighter ions which thus can extract and emit more electrons (cf. discussion below).

Another, more detailed example is shown in Fig. 4, which compares the impact velocity dependences of already published total yields [37] for slow Ne^{10+}, Ar^{10+}, and Xe^{10+} ions, measured with a recoil ion source at GSI, Darmstadt [37]. The solid curves are fits according to an empirically derived relation [37,46],

$$\gamma(v_p) = \frac{c_1}{\sqrt{v_p}} + \gamma_\infty \,, \tag{3}$$

where the dashed lines on the right-hand side of Fig. 4 indicate the respective velocity-independent parts of the yields (i.e., γ_∞) according to Eq. (3).

Ne^{10+}, having the highest total ionization potential $W_{q,\mathrm{pot}} \approx 3600$ eV, obviously gives rise to the highest total electron yield of all three projectile species regarded. Xe^{10+}, on the other hand, with $W_{q,\mathrm{pot}} \approx 800$ eV, emits only about half as many electrons, and the yield for Ar^{10+} ($W_{q,\mathrm{pot}} \approx 1450$ eV) stays in between the values for the two other species. However, the variation of the yield as quantified by the parameter c_1 in Eq. (3) is about twice as high for Xe^{10+} projectiles than for Ne^{10+} in the same velocity range ($2\times10^4 \le v_p \le 1.5\times10^5$ m/s). This difference in the velocity-dependent part of γ cannot be explained within the COB model, because the assumption of "undisturbed" AI transitions between H-like levels is no longer valid for the last phase of the approach of slow Xe^{10+} to a metal surface. Model calculations similar to those presented in Ref. [38] show that a considerable number of electrons can reach the ($n = 5$) and ($n = 6$) shells before the projectile hits the surface. In the case of Xe^{10+}, with its permanently occupied ($n = 4$) levels, one has to expect a strong influence of the ion core to the

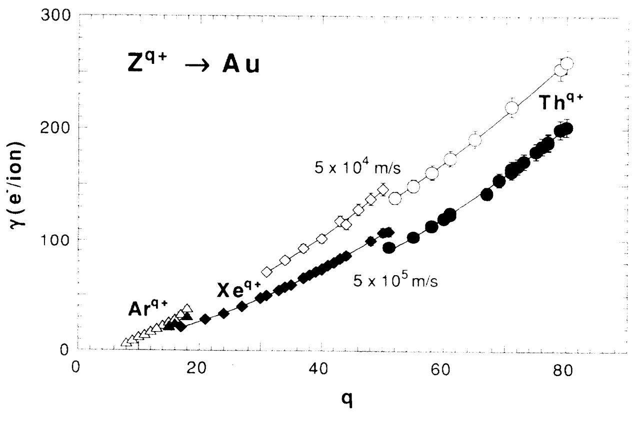

FIG. 3. Total electron yield γ plotted vs ion charge state q for the impact of highly charged Ar (triangles), Xe (diamonds), and Th (circles) ions on clean polycrystalline gold at impact velocities of $v_p \approx 5\times10^4$ m/s (open symbols) and $v_p \approx 5\times10^5$ m/s (full symbols), respectively.

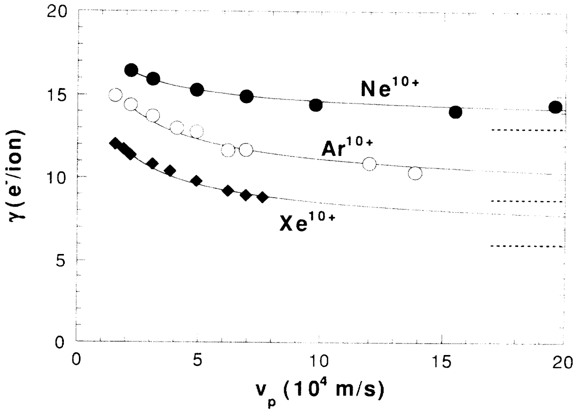

FIG. 4. Total electron yield γ vs projectile velocity for the impact of Ne^{10+}, Ar^{10+}, and Xe^{10+} on clean polycrystalline gold, measured with a recoil ion source at GSI Darmstadt (data from [37,46]). Solid curves are fits according to Eq. (3) to data points for $v_p \ge 2.5\times10^4$ m/s, and dashed lines indicate γ_∞ as the velocity-independent part of the yield.

structure of the ($n=5$) and ($n=6$) levels, which can play an important role in the electron-emission process [AI, peeling off (PO), etc.] just in front, at, and immediately below the surface. However, the probably somewhat smaller number of electrons emitted in the same region due to impact of Ne^{10+} is more than compensated for by the subsequent slow electron contributions from various subsurface processes discussed in the next paragraphs.

B. Total yields vs projectile ionization potential

Figure 5 shows (for $v_p \approx 5\times10^4$ m/s and $v_p \approx 5\times10^5$ m/s) that the total electron yields increase monotonously with the total potential energy $W_{q,\mathrm{pot}}$ [49] related to the projectile ions (see below).

For ions in comparably low charge states, a linear increase of γ with $W_{q,\mathrm{pot}}$ [2–11] can be found as long as the projectiles have initially completely full inner shells [37]. However, towards higher charge states this dependence obviously becomes flatter (cf. Fig. 5). For both Xe^{q+} and Th^{q+} ions, γ approximately follows the square root of the total potential energy carried by the respective projectiles. Discontinuities are found only where, for Xe^{q+} projectiles, L-shell vacancies appear ($q>44$, $W_{q,\mathrm{pot}}>51$ keV). Analysis of the slope of the curves in Fig. 5 shows that the potential energy of a projectile with a still intact L shell is converted into electron emission about three to four times more efficiently (Xe^{40+}–Xe^{44+}, ca. 1.1 keV, and Th^{55+}–Th^{67+}, ca. 1.8 keV, required per emitted electron) than the extra potential energy stored in the projectile L-shell vacancies ($\mathrm{Xe}^{q+}, q>44$, ca. 4 keV/electron). Similar observations have already been made with Ne^{q+} (K-shell vacancies for $q>8$), and Ar^{q+} projectiles (L-shell vacancies for $q>8$, K-shell vacancies for $q=17$, 18; [37]).

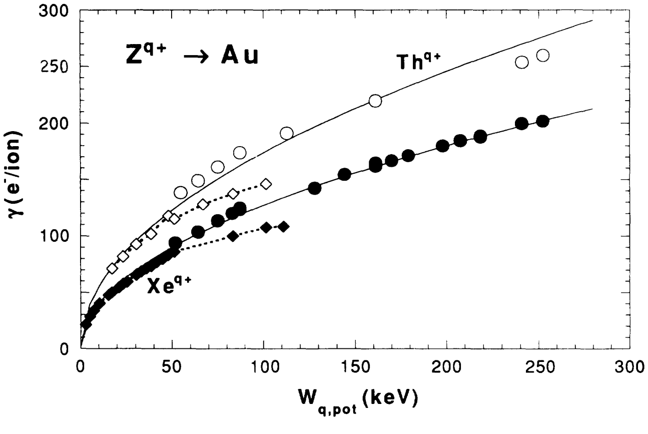

FIG. 5. Total electron yield γ plotted vs total potential energy carried by the projectile ions for the impact of highly charged Xe and Th ions on clean polycrystalline gold at impact velocities of $v_p \approx 5\times10^4$ m/s (open symbols) and $v_p \approx 5\times10^5$ m/s (full symbols), respectively. The yields approximately follow a $\gamma \propto W_{q,\mathrm{pot}}^{1/2}$ dependence with deviations occurring where the projectile starts to carry L-shell vacancies (Xe^{q+}, $q\geq45$ at $W_{q,\mathrm{pot}}\approx50$ keV). Note the discrepancy between data for Th and Xe ions of same $W_{q,\mathrm{pot}}$.

This much less efficient electron emission induced by MCI with inner-shell vacancies is another strong hint for the important role of the projectile's electronic structure. During the limited time between the first electron capture into highly excited projectile states and the impact of the projectile on the surface, deexcitation of the resulting highly excited hollow atoms is apparently too slow to transfer electrons efficiently into inner-shell vacancies. Consequently, there is a good chance for the hollow atoms to arrive at the surface with their initial K or L-shell vacancies still unoccupied. However, as soon as all the electrons in higher n states have been peeled off (see below), the projectile will be rapidly reneutralized and form a modified hollow atom upon penetrating the target surface. This renewed neutralization might involve either resonant capture of target core electrons (with subsequent emission of target Auger electrons) or Auger transitions between projectile and bulk electronic states. Either process may cause emission of comparably fast electrons (e.g., with kinetic energies in the 210 eV range for Ar^{q+}, $q\geq9$, and in the 2.5 keV range for $q\geq17$). These fast so-called subsurface Auger electrons [13,17,18,50,51] might also induce secondary electron emission from the solid. However, all subsurface processes are comparably inefficient in terms of the potential energy to be spent per emitted electron. Qualitatively, their reduced efficiency can be held responsible for the transition from the linear γ vs $W_{q,\mathrm{pot}}$ relation at low q to an approximately linear γ vs q relation for high charge states (cf. Figs. 3 and 5, and Refs. [37] and [51]).

C. Impact velocity dependence of total yields

Figures 6–8 illustrate in some detail the observed dependences of total electron yields on the nominal projectile velocity for differently charged MCI's of Ar, Xe, and Th, respectively. In the velocity range $v_p \geq 3\times10^4$ m/s the velocity dependence is generally quite well repro-

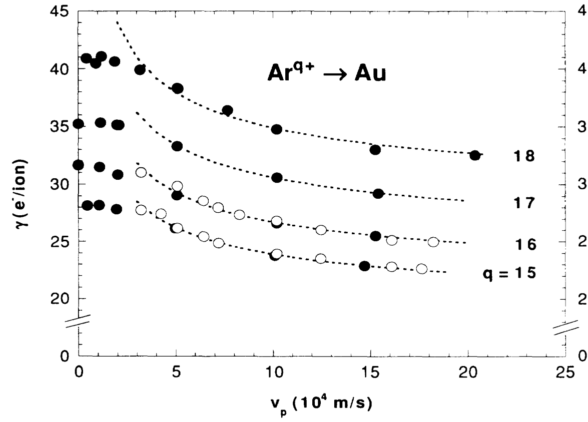

FIG. 6. Total electron yield γ plotted vs nominal (cf. text) projectile velocity for the impact of Ar^{q+} ($q=15$–18) on clean polycrystalline gold. Full symbols refer to data measured at LLNL, open symbols to data taken with a recoil ion source at GSI Darmstadt [37,46]. The dashed lines are fits according to Eq. (3) to data points for $v_p \geq 2.5\times10^4$ m/s.

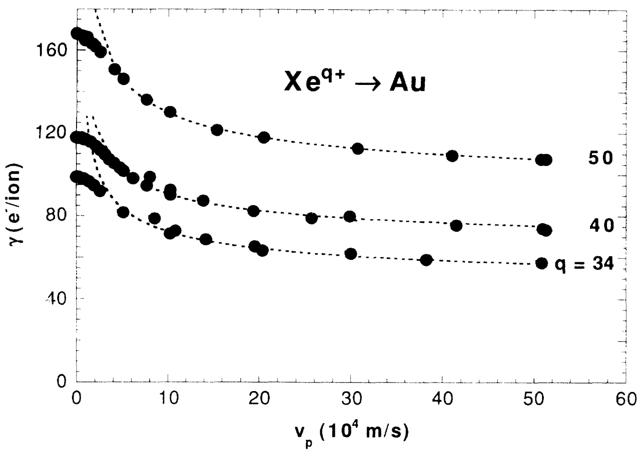

FIG. 7. Total electron yield γ plotted vs nominal (cf. text) projectile velocity for the impact of Xe^{q+} ($q=34$, 40, 50) on polycrystalline gold. The dashed lines are fits according to Eq. (3) to data points for $v_p \geq 2.5\times10^4$ m/s. Note clear deviations from these fits at the lowest impact velocities.

duced by the previously given Eq. (3) (see above), as has been indicated by dashed curves in all three figures.

For impact velocities beyond 10^5 m/s, the velocity dependence becomes rather flat and would tend toward a minimum [7,42] if kinetic electron emission made a non-negligible contribution. However, for the highly charged ions regarded here, this region is far beyond the highest impact velocities applied in the present experiment. Toward the lowest velocities ($v_p \leq 3\times10^4$ m/s), on the other hand, the yields do not further increase steeply as predicted by Eq. (3), because now the acceleration of the ions by their own image charge, formed in the conducting surface until there is complete neutralization, is becoming important. This image charge acceleration sets an upper limit to the available interaction time until surface impact. Consequently, an upper limit is set also for the electron yields if this acceleration clearly dominates the projectile impact energy. Using the onset of this yield stagnation we can obtain the amount of kinetic energy gained due to the image charge acceleration, as will be shown in detail in Sec. III E.

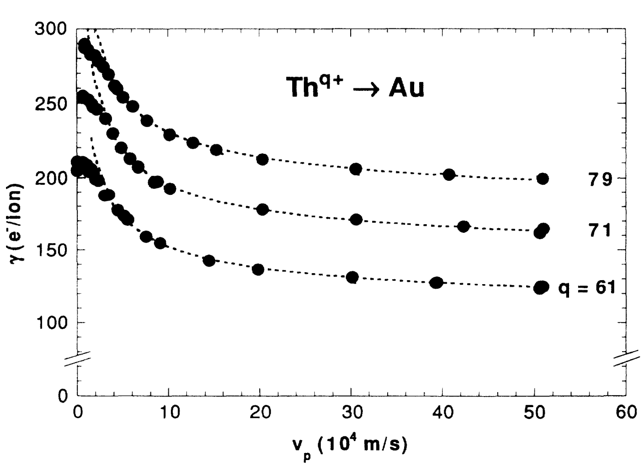

FIG. 8. Same as Fig. 7, for impact of Th^{q+} ($q=61$, 71, 79).

Comparison with results of a simulation shows that the velocity-dependent part of the observed total electron yields [cf. Eq. (3)] can be mainly ascribed to above-surface autoionization [37], whereas γ_∞, the velocity-independent part of the yield, can be ascribed to the process of peeling off and screening and image-shift promotion of electrons above the vacuum level. For projectiles in the highest charge states, we found γ_∞ to be of the order of twice the initial projectile charge state q. Peeling off and screening and image shift probably cannot contribute more than 1.5 q electrons per projectile [38], so that the above discussed subsurface secondary electrons might make up for the increase in the velocity-independent part of the yield.

A simple-minded attempt to derive analytically the velocity dependence of γ would assume constant autoionization rate coefficients for subsequent above-surface AI processes. This would yield the number of emitted electrons proportional to the inverse projectile velocity ($\gamma \propto v_p^{-1}$), reflecting the simple fact that the slower the projectile, the more time it can spend in the interaction region between the first electron capture at R_c and the surface impact, and consequently the more time would be available to extract electrons from the conduction band via RN and then to emit them via AI. From the observed $v_p^{-1/2}$ dependence we conclude that the number of electrons emitted per unit time due to AI processes actually decreases during the approach of the projectile. In fact, with shrinking ion-surface distance the increasing competition of RI with AI will reduce the number of electrons becoming available for the AI processes and thus hamper the further increase of the AI contributions with decreasing impact velocity.

D. Width of ES probability distributions

Besides the total yields, which are equal to the mean values of the ES probability distributions, the measured ES spectra also show characteristic widths. For Xe^{q+} and Th^{q+} projectiles, at a given impact velocity $v_p \approx 5\times10^5$ m/s, we find an almost linear relation between the standard deviations σ of the ES probability distributions (as derived by Gaussian fits, cf. Sec. II) and their mean values γ (Fig. 9). ES distributions measured for lower impact velocities show the same trend, but the corresponding data scatter more than in the case given in Fig. 9, for which the same raw data as for Figs. 3 and 5 have been used.

For Poissonian probability distributions the standard deviation is not a free parameter, but rather $\sigma=\gamma^{1/2}$, cf. solid curve in Fig. 9. For high γ the related Poissonians approach a Gaussian shape. However, the experimentally obtained ES distributions at higher yields ($\gamma > 100$) are broader than Poissonians for the same mean value, i.e., $\sigma_{\mathrm{ES}} > \sigma_{\mathrm{Poisson}}$, whereas for yields $\gamma < 100$ they become narrower. An earlier study with Ar^{q+} projectiles ($q \leq 16$, $\gamma \leq 30$) [38] showed that the ES involved standard deviations of about 85% of the square root of the yields

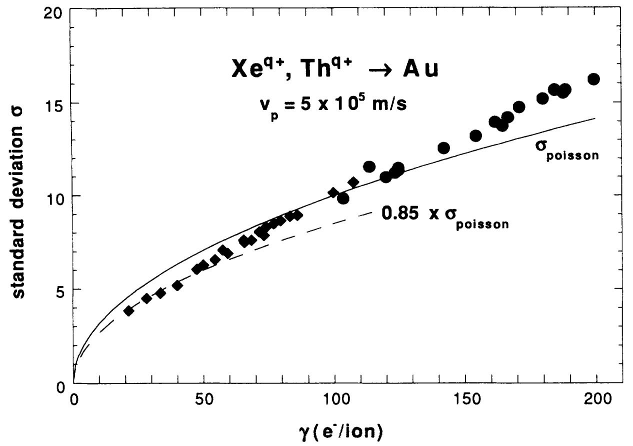

FIG. 9. For Xe and Th projectiles with impact velocity $v_p = 5\times10^5$ m/s, there is a nearly linear relation between the standard deviation σ of the ES probability distribution and its mean value γ. For comparison, the relation between γ and σ for a Poissonian probability distribution ($\sigma=\gamma^{1/2}$) is indicated by a solid line; the dashed line shows the relation $\sigma=0.85\times\gamma^{1/2}$ found earlier for Ar^{q+} projectiles ($q\leq16$) [38].

($\sigma\approx0.85\gamma^{1/2}$). These comparably "narrow" ES have been explained by the contribution from peeling off of a relatively large and rather well defined number ($\approx q$) of electrons still bound in highly excited projectile states at the instant of surface impact.

The relatively broader ES distributions obtained for high γ in the present studies presumably result from two reasons. First, for ions with higher charge q there will be a relatively higher fraction of the above-surface AI processes (cf. velocity dependent parts of γ in Figs. 7 and 8), which were found to provide the main contribution to the ES widths in the model calculations mentioned above [38]. On the other hand, subsurface Auger processes with the subsequent emission of slow secondary electrons from the solid should contribute more efficiently to the total yields, the higher the projectile charge and thus the higher the chance for inner-shell vacancies to survive the projectile's penetration of the surface. Since the subsurface secondary electrons are produced with relatively broad emission probability distributions, they will accordingly contribute to the increased overall widths of the ES probability distributions.

E. Image charge acceleration and distance of first neutralization

The collective dynamical response of the metal conduction electrons to an approaching charged particle in front of the surface can be described by the classical concept of image charge, if the particle does not move too fast and if its distance to the surface remains large compared to the one-electron radius of the conduction-band electrons times the square root of the particle's charge (cf. [34] and references therein). In the present context, where we investigate the effect of the image charge on the movement of slow highly charged ions at comparably large distances in front of a gold surface, these conditions are well satisfied and the classical image charge potential,

$$V_{\rm im}(z) = -\frac{q^2}{4z} \tag{4}$$

(z is the distance to the surface), can be applied to properly describe the interaction of the projectile with the conduction-band electrons. We have to take into account, however, that the ion charge is rapidly diminished during the approach toward the surface, once the critical distance R_c has been passed. Between R_c and the surface the image charge potential—though rapidly decreasing because of the decreasing ion charge—continues to accelerate the projectile toward the surface until it has become completely neutralized. The resulting gain in the projectile's kinetic energy sets a lower limit to the achievable projectile impact velocity and thus limits the resulting total electron emission yield γ (cf. Sec. III C).

Plotting the measured electron yields vs the inverse nominal projectile velocity v_p^{-1} permits the direct evaluation of the gain in impact velocity due to the image charge attraction. Figure 10 exemplifies for Th^{71+} ions how the related minimum impact velocity can be found from the intersection of the saturated yield value and an extrapolation of the yield dependence according to Eq. (3) (dashed curve in Fig. 10), where the parameters c_1 and γ_∞ have already been determined by fits at higher impact velocities. In this particular case the gain in kinetic energy due to image charge attraction, i.e., the principally lowest achievable impact energy $\Delta E_{q,\rm im}$ is found to be 700±160 eV.

As an alternative approach, we might introduce a second term in the denominator in Eq. (3) to account for the image charge acceleration. However, attempts to determine $\Delta E_{\rm im}$ by such a three parameter ($c_1,\gamma_\infty,\Delta E_{\rm im}$) fit to the measured γ vs v_p characteristics turned out to

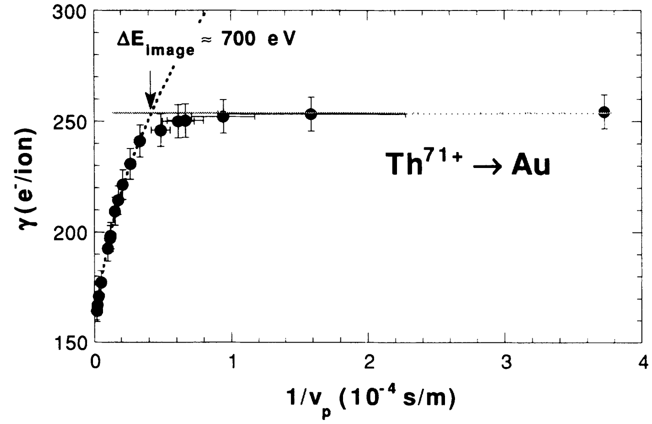

FIG. 10. Total electron yield γ vs inverse nominal projectile velocity $1/v_p$ for impact of Th^{71+} on clean polycrystalline gold (same data as given in Fig. 8). For higher impact velocities ($1/v_p\leq3\times10^{-5}$ s/m), Eq. (3) reproduces the measured data very well (see also Fig. 8), whereas at lower velocities the yields level off towards an apparently constant value. Intersection of this value with data extrapolated according to Eq. (3) permits us to estimate the minimum velocity due to the kinetic-energy gain because of the image charge attraction.

be rather sensitive to the scatter of the relatively small number of data points.

Vertical error bars in Fig. 10 correspond to the mentioned ±4% uncertainty of the total slow electron yields. The horizontal error bars give the uncertainty for determination of the impact velocity, resulting mainly from the limited accuracy of the voltage measurements for finding the projectile's nominal kinetic energy (cf. Fig. 1 and related comments in Sec. II). The error in the voltage measurement is estimated with $\leq \pm 1$ V and thus results in an error of $\leq \pm q$ eV for the nominal kinetic energy of a Z^{q+} projectile. It has to be stressed here that the latter error applies to the uncertainty for the determination of the centroid of the ion-beam energy distributions dN/dE (solid curve in Fig. 1), which defines the zero point for the potential difference between ion source and target. The width of the energy distribution in Fig. 1 is much larger than the uncertainty of its centroid position, but this would be of importance only for rather slow projectiles, where the image charge acceleration rather than the nominal kinetic energy determines the effective velocity of the projectiles during the last part of their trajectory.

With this simple method, impact energy gains due to image charge acceleration have been determined for six different highly charged ion species, and plotted vs projectile charge state q in Fig. 11. In contrast to our present measurements, in other studies for multicharged Ar [52] and Xe [53] ions the image charge acceleration has been determined from the change of the specular projectile scattering angle with respect to a single-crystal target surface bombarded under grazing incidence. Results of these experiments suggested a saturation of image charge acceleration at charge states around $q \approx 30$. Possible explanations for this discrepancy have been proposed in Ref. [51].

Figure 12 illustrates the development of projectile charge (smoothed) and kinetic-energy gain of a Th^{71+} ion approaching a Au surface under the assumption that electrons are immediately captured from the conduction band as soon as condition (1) is satisfied ("staircase" approximation of the COB model). At $R_c \approx 64$ a.u. the ion has already gained about 75% of the image charge acceleration energy (marked by a cross). Inside R_c, electron capture starts, leading to gradual reduction and eventual termination of the acceleration. For sufficiently high q the fraction of image acceleration energy gained before the first electron capture can also be derived analytically from the COB model (cf. Ref. [35]):

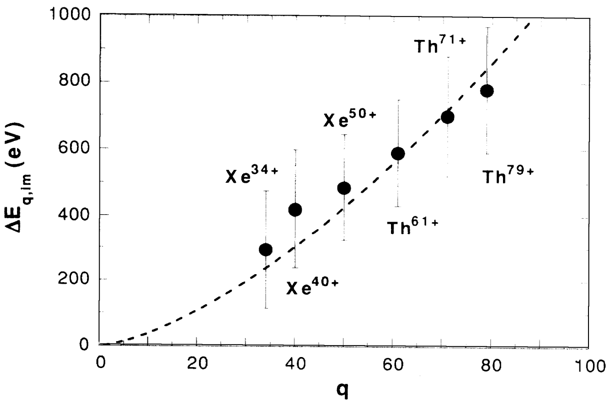

FIG. 11. Kinetic-energy gains $\Delta E_{q,\mathrm{im}}$ due to image charge attraction as determined according to Fig. 10, for impact of highly charged Xe and Th ions (full symbols) on clean polycrystalline gold. The dashed line shows the $q^{3/2}$ dependence of $\Delta E_{q,\mathrm{im}}$ as predicted by the COB model.

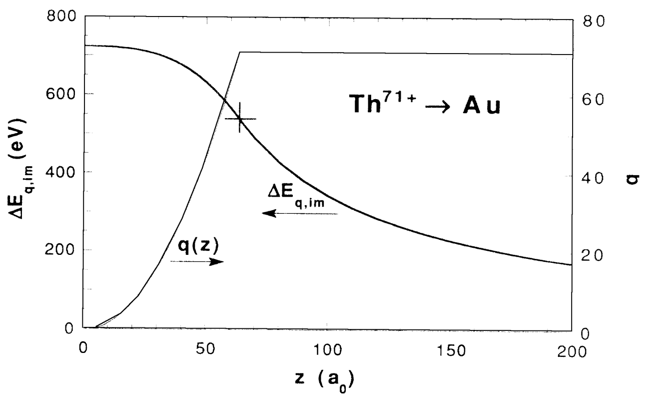

FIG. 12. Instantaneous charge state q (thin solid curve) and related energy gain because of image charge acceleration (bold solid curve) of a Th^{71+} ion approaching a clean gold surface. For determining the evolution of the charge states, the staircase approximation of the COB model has been used. Before the first electrons are captured at a distance $R_c \approx 64$ a.u. (indicated by a cross), the ion has already gained about 75% of its total kinetic-energy gain due to image charge acceleration.

$$\Delta E = \tfrac{3}{4}\Delta E_{q,\mathrm{im}} = \frac{q^2}{4R_c} = \frac{q^2 2W_\Phi}{4\sqrt{8q}+2} \approx \frac{W_\Phi}{4\sqrt{2}} q^{3/2} . \quad (5)$$

For a gold target (work function $W_\Phi = 5.1$ eV ≈ 0.188 a.u.), ΔE amounts to approximately $0.033q^{3/2}$ a.u. In addition, an energy of about $0.011q^{3/2}$ a.u. will be gained during the ongoing neutralization between R_c and surface impact. Therefore, a projectile with initial charge q should gain a total additional energy $\Delta E_{q,\mathrm{im}}$ due to image charge acceleration in front of a Au surface of about $0.044q^{3/2}$ a.u. (dashed curve in Fig. 11). Within our still considerable error margins the values of $\Delta E_{q,\mathrm{im}}$ as derived from the measured impact velocity dependence of γ are reproduced by this curve quite well.

Because the projectiles experience the major part of their image charge acceleration already before their neutralization has started, details of the subsequent neutralization processes are not very decisive for the total amount of energy gained. Therefore, one can utilize Eq. (5) to estimate the distance R_c of first electron transfer from the measured image charge acceleration.

$$R_c \approx \frac{q^2}{3\Delta E_{q,\mathrm{im}}} \quad (5a)$$

The results are presented in Fig. 13 together with the prediction of the COB model according to Eq. (1), and show

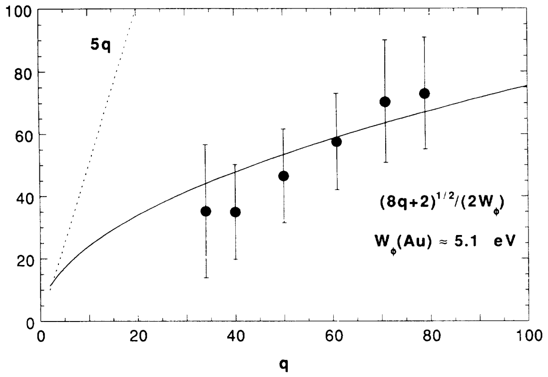

FIG. 13. By assuming that the projectile gains approximately 75% of the image charge acceleration $\Delta E_{q,\mathrm{im}}$ before it will capture the first electrons, and only the remaining 25% during its subsequent neutralization sequence, one can estimate the critical distance R_c for first electron capture from the obtained energy gain $\Delta E_{q,\mathrm{im}}$ of the ions. The such derived values for R_c correspond, within the given errors, with the prediction of the COB model [cf. Eq. (1)].

fairly satisfactory agreement between experimental data and theoretical expectations. An earlier model (dashed line) developed for ions in lower charge states [54] obviously fails for the here investigated, much higher charged ions.

IV. CONCLUSIONS

Our technique of measuring the statistics of MCI-inducted electron emission from metal surfaces precisely determines total electron yields and widths of the related probability distributions for very low fluxes of projectile ions. In combination with a source of extremely highly charged ions like EBIT, the range of these measurements could be extended for slow projectile ions to the highest slow ion charge states available today.

We found most of the trends already observed with projectiles in low and medium charge states ($q \leq 25$) to continue up to the much higher q covered in the present study. In particular, no saturation of the total electron yield is found with further increasing charge state and/or total potential energy carried by the projectile. The impact velocity dependence of the total yields γ and some features of the dependence of γ on the projectiles's total potential energy and of the width of the ES distributions provide conclusive evidence that the deexcitation of the intermediate hollow atoms cannot be completed above the surface and that subsurface neutralization and deexcitation play an increasingly important role for very highly charged ions approaching a metal surface.

From the velocity dependence of γ we can also estimate the amount of kinetic energy which a slow MCI gains due to the attraction by its own image charge in front of a metal surface. We find reasonable agreement with predictions of the semiclassical COB model for image acceleration energies as well as for the related distances of first electron capture.

ACKNOWLEDGMENTS

The authors wish to express their gratitude to the staff of Lawrence Livermore Laboratory for providing excellent working conditions for the present experiments. Work has been performed under the auspices of the U.S. Department of Energy by Lawrence Livermore National Laboratory under Contract No. W-7405-ENG-48 and has been supported by Austrian Fonds zur Förderung der wissenschaftlichen Forschung (Projekt Nr. P8315TEC), and by Kommission zur Koordination der Kernfusionsforschung at the Austrian Academy of Sciences.

[1] P. Varga and HP. Winter, in *Particle Induced Electron Emission II,* edited by G. Höhler (Springer, Heidelberg, 1992), Vol. 123, p. 149.

[2] H. D. Hagstrum, Phys. Rev. **96**, 325 (1954).

[3] H. D. Hagstrum, Phys. Rev. **96**, 336 (1954).

[4] H. D. Hagstrum and G. E. Becker, Phys. Rev. B **8**, 107 (1973).

[5] U. A. Arifov, E. S. Mukhamadiev, E. S. Parilis, and A. S. Pasyuk, Zh. Tekh. Fiz. **43**, 181 (1973) [Sov. Phys. Tech. Phys. **18**, 118 (1973)].

[6] M. Delaunay, S. Dousson, R. Geller, P. Varga, M. Fehringer, and HP. Winter, in *Abstracts of Contributed Papers, 14th International Conference on the Physics of Electronic and Atomic Collisions, Palo Alto 1985,* edited by M. J. Coggiola *et al.* (North-Holland, Amsterdam, 1986), p. 477.

[7] M. Delaunay, M. Fehringer, R. Geller, D. Hitz, P. Varga, and HP. Winter, Phys. Rev. B **35**, 4232 (1987).

[8] M. Fehringer, M. Delaunay, R. Geller, P. Varga, and HP. Winter, Nucl. Instrum. Methods Phys. Res. Sect. B **23**, 245 (1987).

[9] M. Delaunay, M. Fehringer, R. Geller, P. Varga, and HP. Winter, Europhys. Lett. **4**, 377 (1987).

[10] S. T. de Zwart, Ph.D. thesis, Rijksuniversiteit Groningen (1987).

[11] S. T. de Zwart, A. G. Drentje, A. L. Boers, and R. Morgenstern, Surf. Sci. **217**, 298 (1989).

[12] D. M. Zehner, S. H. Overbury, C. C. Havener, F. W. Meyer, and W. Heiland, Surf. Sci. **178**, 359 (1986).

[13] F. W. Meyer, S. H. Overbury, C. C. Havener, P. A. Zeijlmans van Emmichhoven, and D. M. Zehner, Phys. Rev. Lett. **67**, 723 (1991).

[14] F. W. Meyer, S. H. Overbury, C. C. Havener, P. A. Zeijlmans van Emmichhover, J. Burgdörfer, and D. M. Zehner, Phys. Rev. A **44**, 7214 (1991).

[15] P. A. Zeijlmans van Emmichoven, C. C. Havener, I. G. Hughes, D. M. Zehner, and F. W. Meyer, Phys. Rev. A **44**, 4214 (1993).

[16] L. Folkerts and R. Morgenstern, Europhys. Lett. **13**, 377 (1990).

[17] J. Das and R. Morgenstern, Phys. Rev. A **47**, R755 (1993).

[18] J. Das, L. Folkerts, and R. Morgenstern, Phys. Rev. A **45**, 4669 (1993).

[19] R. Köhrbrück, K. Sommer, J. P. Biersack, J. Bleck-

Neuhaus, S. Schippers, P. Roncin, D. Lecler, F. Fremont, and N. Stolterfoht, Phys. Rev. A **45**, 4653 (1992).

[20] S. Schippers, S. Hustedt, W. Heiland, R. Köhrbrück, J. Bleck-Neuhaus, J. Kemmler, D. Lecler, and N. Stolterfoht, Phys. Rev. A **46**, 4003 (1992).

[21] E. D. Donets, Phys. Scr. **T3**, 11 (1983).

[22] E. D. Donets, Nucl. Instrum. Methods Phys. Res. Sect. B **9**, 522 (1985).

[23] J. P. Briand, L. de Billy, P. Charles, S. Essabaa, P. Briand, R. Geller, J. P. Desclaux, S. Bliman, and C. Ristori, Phys. Rev. Lett. **65**, 159 (1990).

[24] M. Schulz, C. L. Cocke, S. Hagmann, M. Stöckli, and H. Schmidt-Böcking, Phys. Rev. A **44**, 1653 (1991).

[25] H. J. Andrä, *et al.*, in *Proceedings of the 17th International Conference on the Physics of Electronic and Atomic Collisions,* Brisbane, Australia, 1991, edited by W. R. MacGillivray, I. E. McCarty, and M. C. Standage (Institute of Physics, London, 1991), p. 89.

[26] M. W. Clark, D. Schneider, D. Dewitt, J. W. McDonald, R. Bruch, U. I. Safranova, I. Y. Tolstikhina, and R. Schuch, Phys. Rev. A **47**, 3983 (1993).

[27] S. T. de Zwart, T. Fried, U. Jellen, A. L. Boers, and A. G. Drentje, J. Phys. B **18**, L623 (1985).

[28] S. T. de Zwart, T. Fried, D. O. Boerma, R. Hoekstra, A. G. Drentje, and A. L. Boers, Surf. Sci. **177**, L939 (1986).

[29] P. Varga, Appl. Phys. A **44**, 31 (1987).

[30] P. Varga, Comments At. Mol. Phys. **27**, 111 (1989).

[31] H. J. Andrä, in *Physics of Highly-IonizedAtoms,* edited by R. Marrus (Plenum, New York, 1989), Vol. 201, p. 377.

[32] H. J. Andrä, Nucl. Instrum. Methods Phys. Res. Sect. B **43**, 306 (1989).

[33] D. Schneider, M. A. Briere, J. W. McDonald, and J. Biersack, Radiat. Eff. Def. Solids **127**, 113 (1993).

[34] J. Burgdörfer, P. Lerner, and F. W. Meyer, Phys. Rev. A **44**, 5674 (1991).

[35] J. Burgdörfer and F. W. Meyer, Phys. Rev. A **47**, R20 (1993).

[36] J. Burgdörfer, in *Fundamental Processes and Applications of Atoms and Ions,* edited by C. D. Lin (World Scientific, Singapore, 1993).

[37] H. Kurz, F. Aumayr, C. Lemell, K. Töglhofer, and HP. Winter, Phys. Rev. A **48**, 2182 (1993).

[38] H. Kurz, F. Aumayr, C. Lemell, K. Töglhofer, and HP. Winter, Phys. Rev. A **48**, 2192 (1993).

[39] G. Lakits, F. Aumayr, and HP. Winter, Rev. Sci. Instrum. **60**, 3151 (1989).

[40] G. Lakits, F. Aumayr, M. Heim, and HP. Winter, Phys. Rev. A **42**, 5780 (1990).

[41] F. Aumayr, G. Lakits, and HP. Winter, Appl. Surf. Sci. **47**, 139 (1991).

[42] K. Töglhofer, F. Aumayr, and HP. Winter, Surf. Sci. **281**, 143 (1993).

[43] R. E. Marrs, M. A. Levine, D. A. Knapp, and J. R. Henderson, Phys. Rev. Lett. **60**, 1715 (1988).

[44] D. Schneider *et al.*, Phys. Rev. A **42**, 3889 (1990).

[45] D. Schneider, M. W. Clark, B. Penetrante, J. W. McDonald, D. DeWitt, and J. N. Bardsley, Phys. Rev. A **44**, 3119 (1991).

[46] H. Kurz, K. Töglhofer, HP. Winter, F. Aumayr, and R. Mann, Phys. Rev. Lett. **69**, 1140 (1992).

[47] H. Kulenkampff and W. Spyra, Z. Phys. **137**, 416 (1954).

[48] F. Aumayr, H. Kurz, D. Schneider, M. A. Briere, J. W. McDonald, C. E. Cunningham, and HP. Winter, Phys. Rev. Lett. **71**, 1943 (1993).

[49] M. Chen (private communication).

[50] I. G. Hughes, J. Burgdörfer, L. Folkerts, C. C. Havener, S. H. Overbury, M. T. Robinson, D. M. Zehner, P. A. Zeijlmans van Emmichhoven, and F. W. Meyer, Phys. Rev. Lett. **71**, 291 (1993).

[51] F. Aumayr and HP. Winter, Comments At. Mol. Phys. **29**, 275 (1994).

[52] H. Winter, Europhys. Lett. **18**, 207 (1992).

[53] H. Winter, C. Auth, R. Schuch, and E. Beebe, Phys. Rev. Lett. **71**, 1939 (1993).

[54] P. Apell, Nucl. Instrum. Methods Phys. Res. Sect. B **23**, 245 (1987).